Supplementary Information

4D visualization of the light-induced coherent magnon by an X-ray free electron laser

Hoyoung Jang[1,2], Hiroki Ueda[3], Hyeong-Do Kim[1], Minseok Kim[1], Kwang Woo Shin[4], Kee Hoon Kim[4], Sang-Youn Park[1], Hee Jun Shin[1], Pavel Borisov[5,6], Matthew J. Rosseinsky[6], Dogeun Jang[1], Hyeongi Choi[1], Intae Eom[1,2], Urs Staub[3] and Sae Hwan Chun[1,2]*

[1]*Pohang Accelerator Laboratory, Pohang, Gyeongbuk 37673, Republic of Korea*

[2]*Photon Science Center, POSTECH, Pohang, Gyeongbuk 37673, Republic of Korea*

[3]*Swiss Light Source, Paul Scherrer Institute, 5232 Villigen-PSI, Switzerland*

[4]*Center for Novel States of Complex Materials Research, Department of Physics and Astronomy, Seoul National University, Seoul 08826, Republic of Korea*

[5]*Department of Physics, Loughborough University, Loughborough, LE11 3TU, United Kingdom*

[6]*Department of Chemistry, University of Liverpool, Liverpool, L7 3NY, United Kingdom*

* Corresponding author: pokchun81@postech.ac.kr

Contents

1. Transient intensity of (0 0 3) reflection at non-resonant photon energy

The resonant FM (0 0 3) Bragg peak contains structure factors not only from the FM component of the canted AFM structure, but also from the crystal structure and orbital asphericity. If the oscillation in the transient (0 0 3) intensity would arise from a coherent phonon, we expect to see the oscillation from the crystal structure contribution at a non-resonant condition, where the magnetic contribution is absent. The incident X-ray photon energy was tuned to E_i = 652 eV away from the X-ray absorption edges of the atomic elements constructing the BSZFAO. We observed no pronounced oscillation in the transient (0 0 3) Bragg peak intensity, but substantial intensity decrease after ~10 ps, which is saturated after ~50 ps (Supplementary Fig. 3). This intensity change shows a monotonic dependence with the fluence, indicative of photo-induced thermal effects with a combination of the Debye-Waller factor and the peak shift. This clearly supports our interpretation that the oscillations observed at the resonance are manifestation of a coherent magnon.

2. Time scale of the lattice thermalization

The FM (0 0 3) Bragg peak contains the crystal structure factor. Its profile of θ - 2θ scan serves as an indicator of the lattice change. Supplementary Figs. 4b & c show time-delay dependence of the peak shifts and widths obtained by fits to a Lorentzian for the θ - 2θ scans shown in Supplementary Fig. 4a. The Bragg peak shifts to a lower angle after ~10 ps, which manifests a lattice expansion. The width rapidly increases around the same time delay, indicating sizable strain gradient during the lattice expansion. The lattice expansion and the strain gradient imply that the lattice thermalization starts from the time delay ~10 ps.

3. Laser fluence and temperature dependence of the AFM magnon precession

The transient changes of normalized FM (0 0 3) Bragg intensities are presented in Supplementary Figs. 5a & b for various laser fluences. The intensities measured at E_i = 702 eV display the nearly identical oscillation profile compared to those observed at resonance on top of the background that decreases with the fluence raised up to 8.0 mJ/cm^2. The oscillation frequency = 41.7 GHz is maintained as shown in the Fourier transformation of the transient intensities (Supplementary Fig. 5d). On the other hand, the intensities measured at E_i = 711 eV exhibit an additional slower oscillation above 2.3 mJ/cm^2. This oscillation becomes progressively dominant with the fluence increased up to 7.4 mJ/cm^2. The presence of two oscillation components and their evolution are evident in their Fourier transformation (Supplementary Fig. 5e). Meanwhile, the overall intensities decrease substantially as the photoinduced increase of lattice temperature affects and melts the transverse conical magnetic order.

The oscillation profile of the transient FM (0 0 3) Bragg intensity was also checked while increasing the sample temperature (Supplementary Fig. 5c). As temperature increases, the crest of the oscillation starts to shift to a longer time delay and this phase shift evolves into a half cycle shift of a sinusoidal profile at 240 K. This shift is attributed to a new spin equilibrium position distinct from that at lower temperatures. In addition, we notice that the oscillation period gradually increases with the temperature elevated (Supplementary Fig. 5f).

4. Magnetic Bragg peak intensities measured by resonant magnetic X-ray diffraction

The incident X-ray in the horizontal scattering geometry has π-polarization, while the scattered X-ray at magnetic Bragg reflections has both π'- and σ'-polarizations. The magnetic Bragg peak intensities are the sum of the individual intensities from the π-π' and π-σ' channels viewing FM (or AFM) moment, $\overrightarrow{M}$:

$$I = I_{\pi-\sigma'} + I_{\pi-\pi'},$$

$$I_{\pi-\sigma'} = B(\vec{k}_i \cdot \overrightarrow{M})^2,$$

$$I_{\pi-\pi'} = B(\vec{k}_f \times \vec{k}_i \cdot \overrightarrow{M} + C)^2,$$

where $\vec{k}_i$ and $\vec{k}_f$ are the incident and scattered X-ray wavevectors, respectively, B is a constant of proportionality, and C is isotropic charge-scattering/orbital-scattering amplitudes. The C has finite values only for FM (0 0 3*n*) (*n*: integer) peaks.

The magnetic Hamiltonian model (*Eq*. 1 in the main text) elucidates the directions of μ_L and μ_S with canted angles ϕ and α from the *x* and *z* axes, respectively. It is determined that $\phi = 60^\circ$ and $\alpha = 30^\circ$ at H_{ext} (|| +*x*) = 200 mT. We take into account this magnetic structure to simulate the oscillations in the magnetic Bragg peak intensities. The notion that the magnitude of μ_L is significantly larger than that of μ_S and contributes more to the magnetic structure factors for both FM and AFM Bragg reflections leads us to build an effective magnon precession model considering only μ_{L1} and μ_{L2}. Before the photoexcitation, the μ_{L1} and μ_{L2} form the canted AFM structure with the FM ($\boldsymbol{m} = \boldsymbol{\mu}_{L1} + \boldsymbol{\mu}_{L2}$) and AFM ($\boldsymbol{l} = \boldsymbol{\mu}_{L1} - \boldsymbol{\mu}_{L2}$) components along the *x* and *y* axes in the *ab* plane, respectively as shown in Supplementary Fig. 6. The precession of $\boldsymbol{\mu}_L$ is projected on the $\boldsymbol{m}$ and $\boldsymbol{l}$ that modulate the magnetic Bragg peak intensities.

5. Inspection of allowed coherent magnon precessions in the BSZAFO

First of all, we examine a case that the photoexcitation induces periodic modulation of the μ_L magnitude rather than angular change (precession). In this case, both FM and AFM Bragg peak intensities are expected to modulate in the same phase, which turn out inconsistent with the observation in Fig. 2 (the main text). Hereafter, we inspect the magnon precessions allowed in the BSZFAO, including FM and AFM magnons, to find the one that accounts for the observed distinct oscillations in the FM and AFM intensities.

Supplementary Figs. 7-10 summarize the available precessions that display distinct oscillation and transient behaviours of the FM and AFM Bragg reflections. We consider the μ_{L1} and μ_{L2}

precessions around quasi-equilibrium directions denoted as μ_{L1}' and μ_{L2}' with various conditions: (1) μ_{L1}' and μ_{L2}' moved out of the *xy* plane (= *ab* plane) or within the plane, (2) the same or opposite directional changes of μ_{L1}' and μ_{L2}', (3) clockwise or counter-clockwise μ_{L1} precession, and (4) FM or AFM magnon precessions of the μ_{L1} and μ_{L2}. For the simulation, each angle between μ_{L1} and μ_{L1}', and between μ_{L2} and μ_{L2}' is set to be 3° with the precession period = 24 ps. Among these conditions, only the case illustrated in Supplementary Fig. 10a (also Fig. 2f in the main text) shows the behaviours consistent with the experimental results observed for the FM (0 0 3) and AFM (0 0 4.5) Bragg reflections. This situation with slight demagnetization (= 5 %) considered also matches the behaviour of the AFM (0 0 1.5) reflection.

6. Coherent magnon excited by the pump laser with *p*- and *s*-polarizations

The AFM (0 0 1.5) Bragg peak shows the intensity oscillations coming from the coherent magnon by the laser pump with *p*- and *s*-polarizations, respectively (Supplementary Fig. 11). The *Eq.* 2 in the main text predicts presence of the photoinduced, effective magnetic-field for both cases of polarizations, which is consistent with the observation in Supplementary Fig. 11.

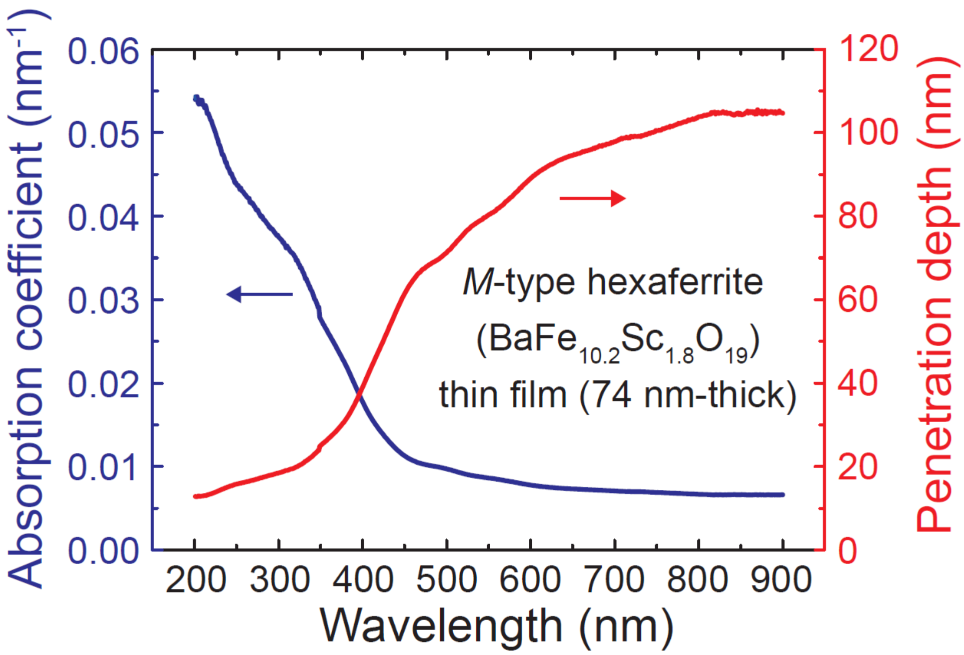

Supplementary Fig. 1| Absorption coefficients and penetration depths of a M-type hexaferrite thin film ($BaFe_{10.2}Sc_{1.8}O_{19}$). The epitaxial film with thickness = 74 nm was grown on the Al_2O_3 (00.1) substrate.

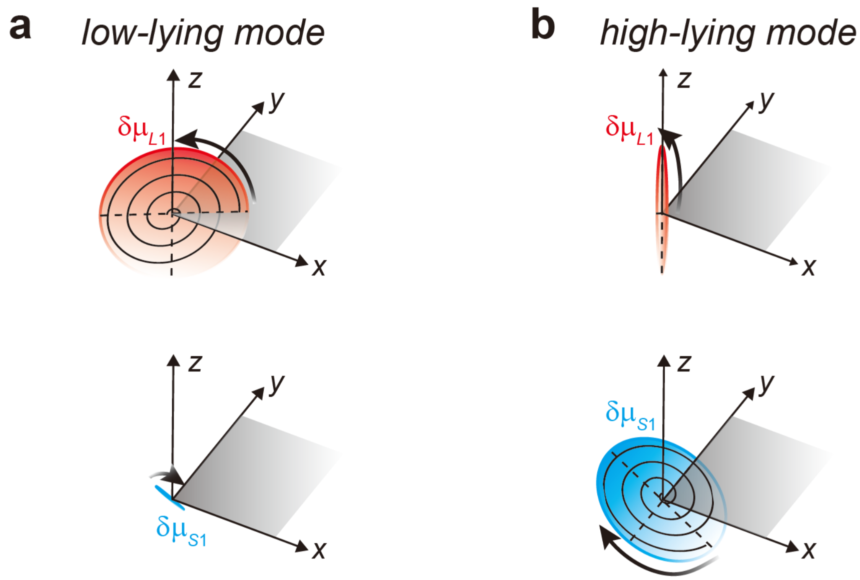

Supplementary Fig. 2| Relative magnitudes of the AFM magnons calculated from the magnetic Hamiltonian. (**a**) The lower energy magnon**.** (**b**) The higher energy magnon. The precession magnitude is normalized by the *z* axis-component of $\delta\mu_{L1}$. The curved black arrows denote the precession directions.

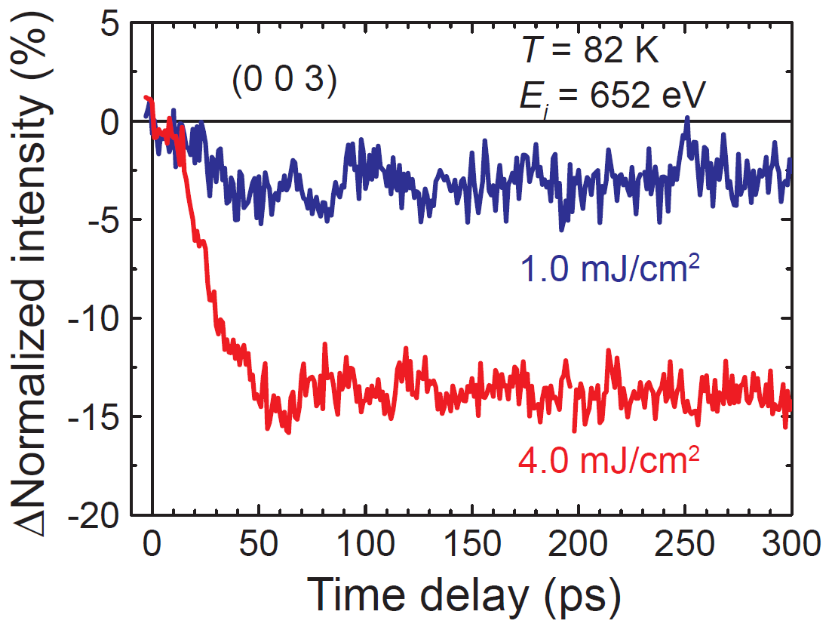

Supplementary Fig. 3| Transient change of the normalized (0 0 3) Bragg peak intensity at a non-resonant condition, E_i = 652 eV. The data were obtained for the laser fluences = 1.0 (blue) and 4.0 mJ/cm^2 (red) at T = 82 K under H_{ext} = 200 mT applied along the x axis in the ab plane.

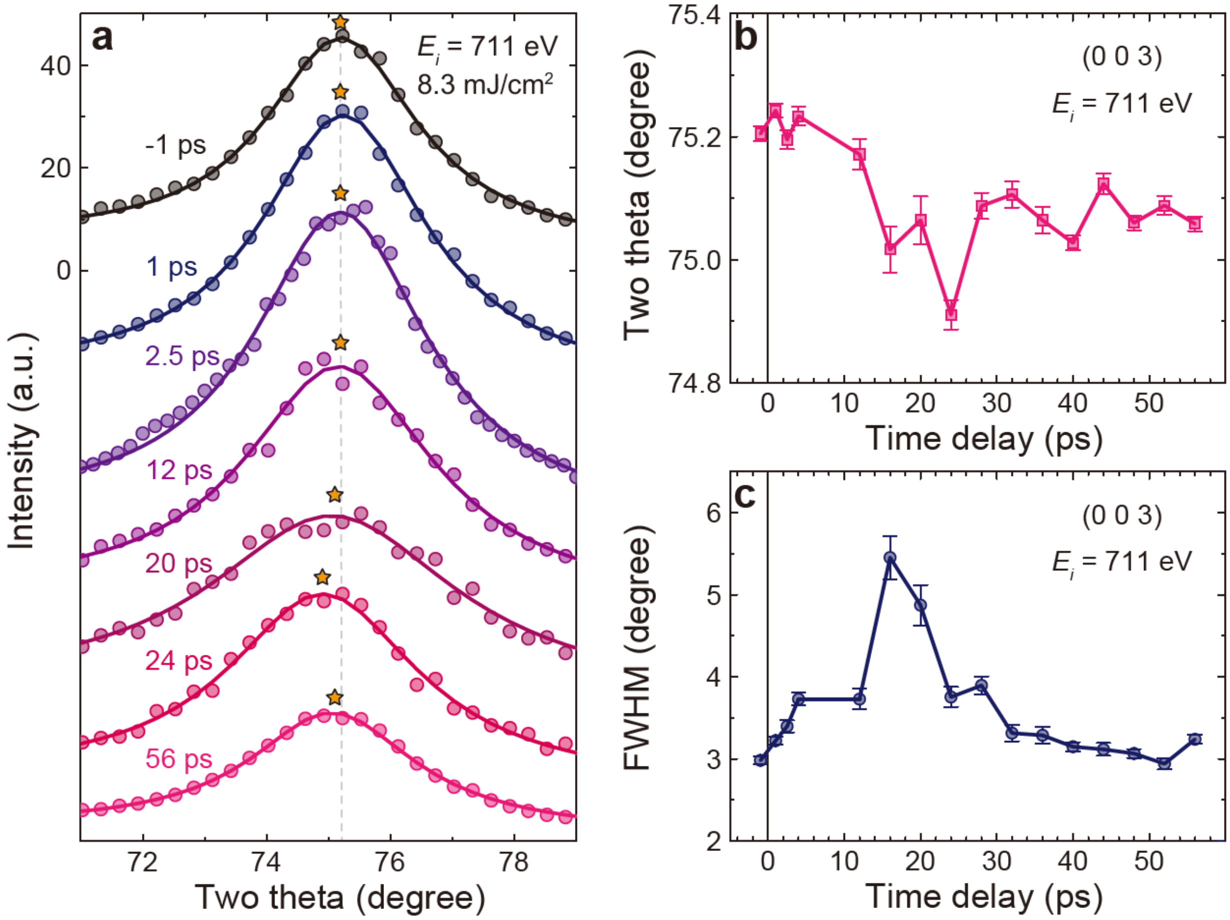

Supplementary Fig. 4| θ - 2θ scans of the (0 0 3) reflection taken at *T* = 82 K for high laser fluence = 8.3 mJ/cm^2 at selected time delays. (**a**) The data (circle) fit with the Lorentzian profile (solid line) are vertically shifted for clarity. Each peak position is indicated by the star symbol. The vertical dashed line depicts the peak position at the time delay = -1 ps. Time dependence of the peak position (**b**) and peak width (**c**) in full-width-at-half-maximum obtained from the fits as a function of time delay.

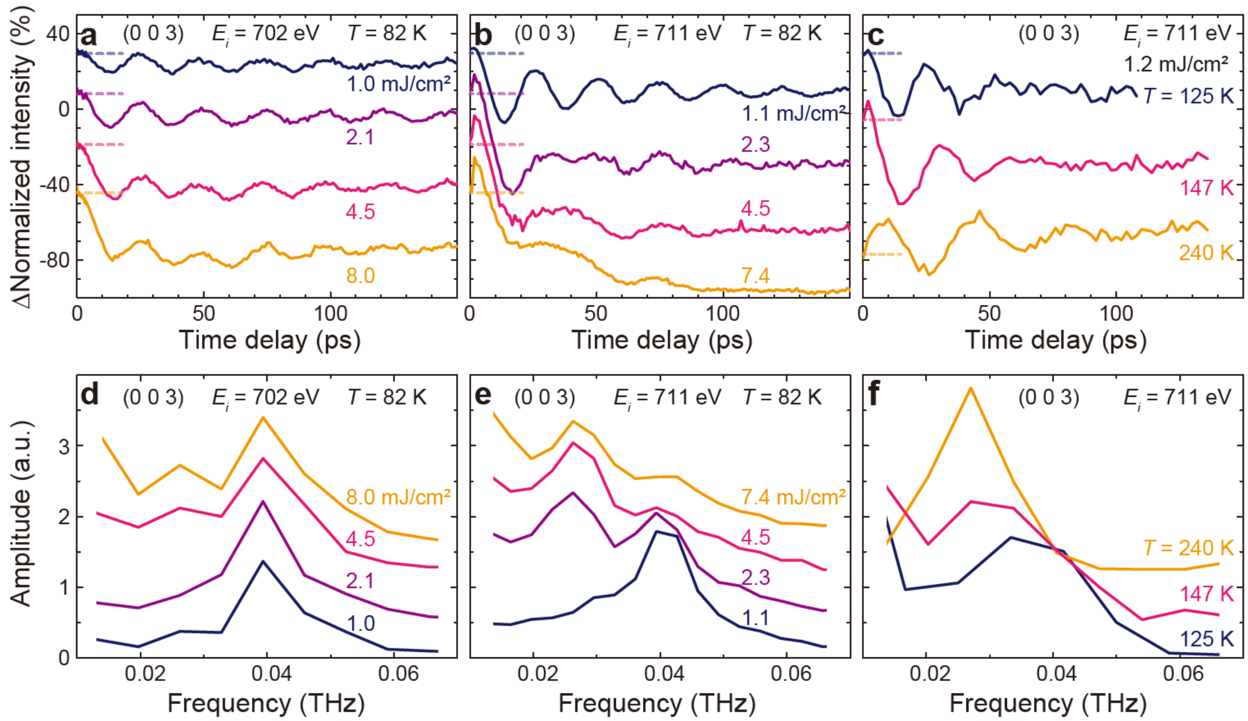

Supplementary Fig. 5| Laser fluence and temperature dependences of transient change of the normalized FM (0 0 3) intensity. Laser fluence dependence of the normalized intensity change at T = 82 K for E_i = 702 eV (**a**) and 711 eV (**b**). (**c**) Temperature dependence of the traces for 1.2 mJ/cm^2 and taken at E_i = 711 eV. The data for each fluence and temperature are vertically shifted for clarity. The shifted base lines are indicated on the left side with dashed lines. (**d**-**f**) Fast Fourier transform of the intensities in (**a**-**c**). The transformed data are vertically shifted for clarity.

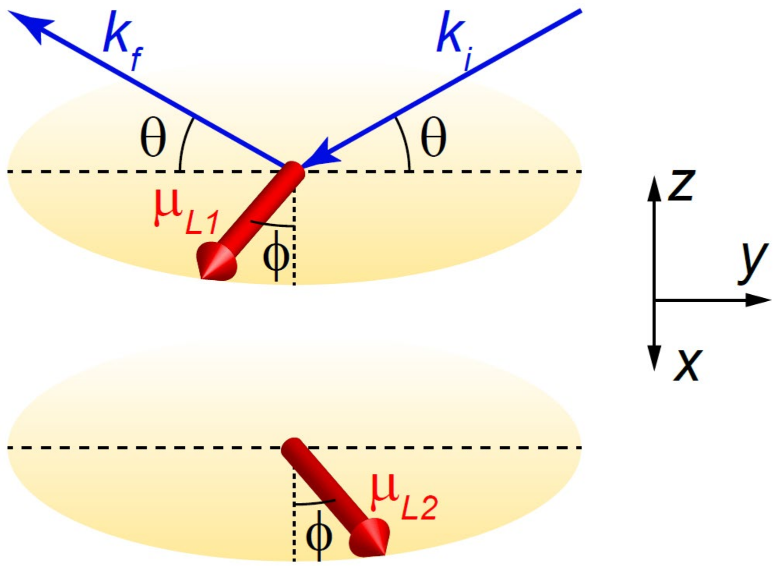

Supplementary Fig. 6| Schematic illustration of the canted AFM structure consisting of μ_{L1} and μ_{L2}.

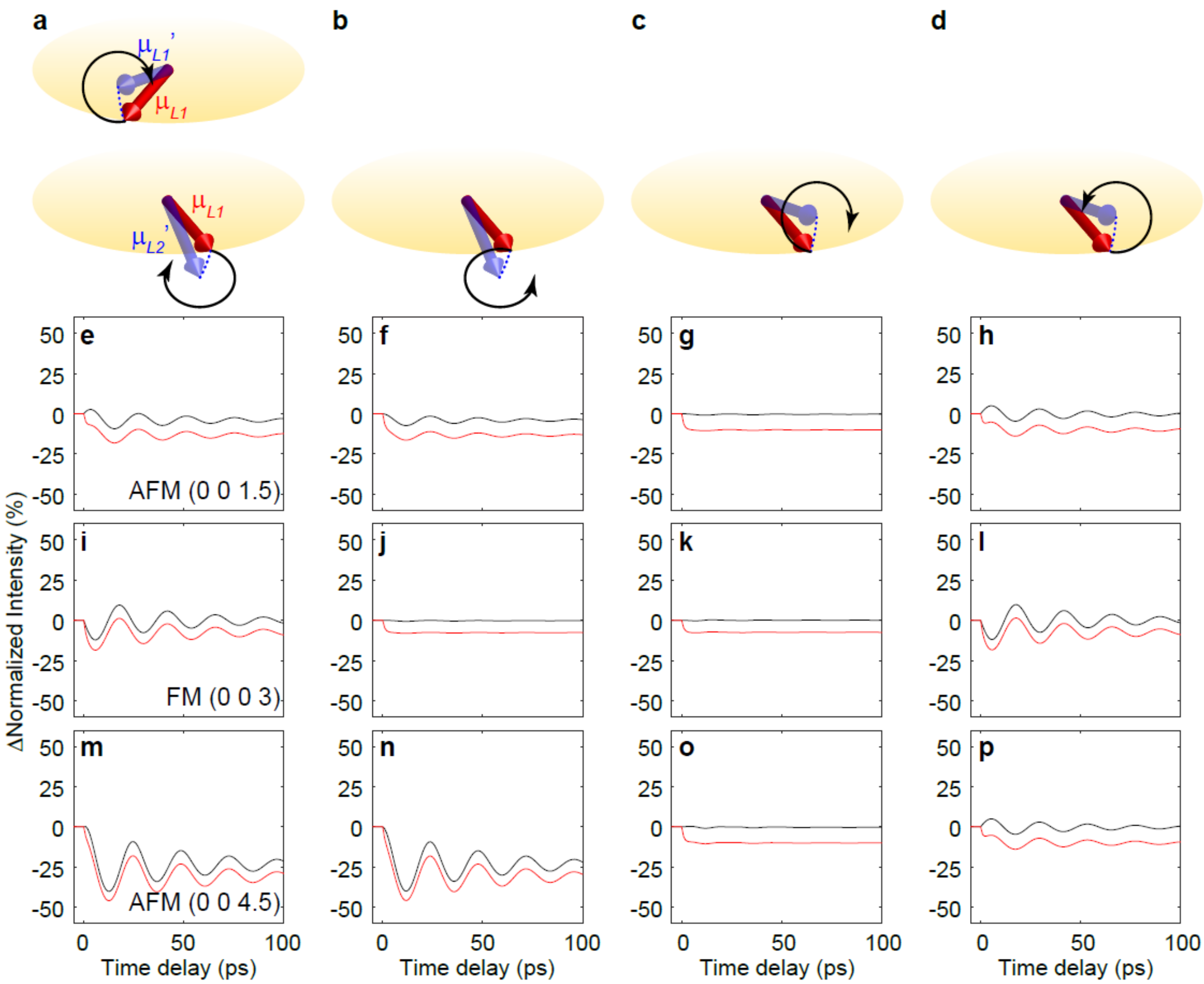

Supplementary Fig. 7| Simulated transient behaviours of the FM and AFM Bragg reflections for the case where μ_{L1} precesses clockwise around a new quasi-equilibrium μ_{L1}' direction located out of the *xy* plane. (**a**) Clockwise and (**b**) counter-clockwise μ_{L2} precessions around μ_{L2}' moved opposite to μ_{L1}' along the *z* axis. (**c**) Clockwise and (**d**) counter-clockwise μ_{L2} precessions around μ_{L2}' moved in the same direction with μ_{L1}' along the *z* axis. The red, blue, and black arrows denote μ_L, μ_L', and precession directions, respectively. The transient intensities of (**e-h**) AFM (0 0 1.5), (**i-l**) FM (0 0 3), and (**m-p**) AFM (0 0 4.5) Bragg peaks for the cases illustrated in (**a-d**), respectively. The intensities are normalized with the one at a negative time delay. Black (red) curves present the simulation results without (with) initial demagnetization, respectively.

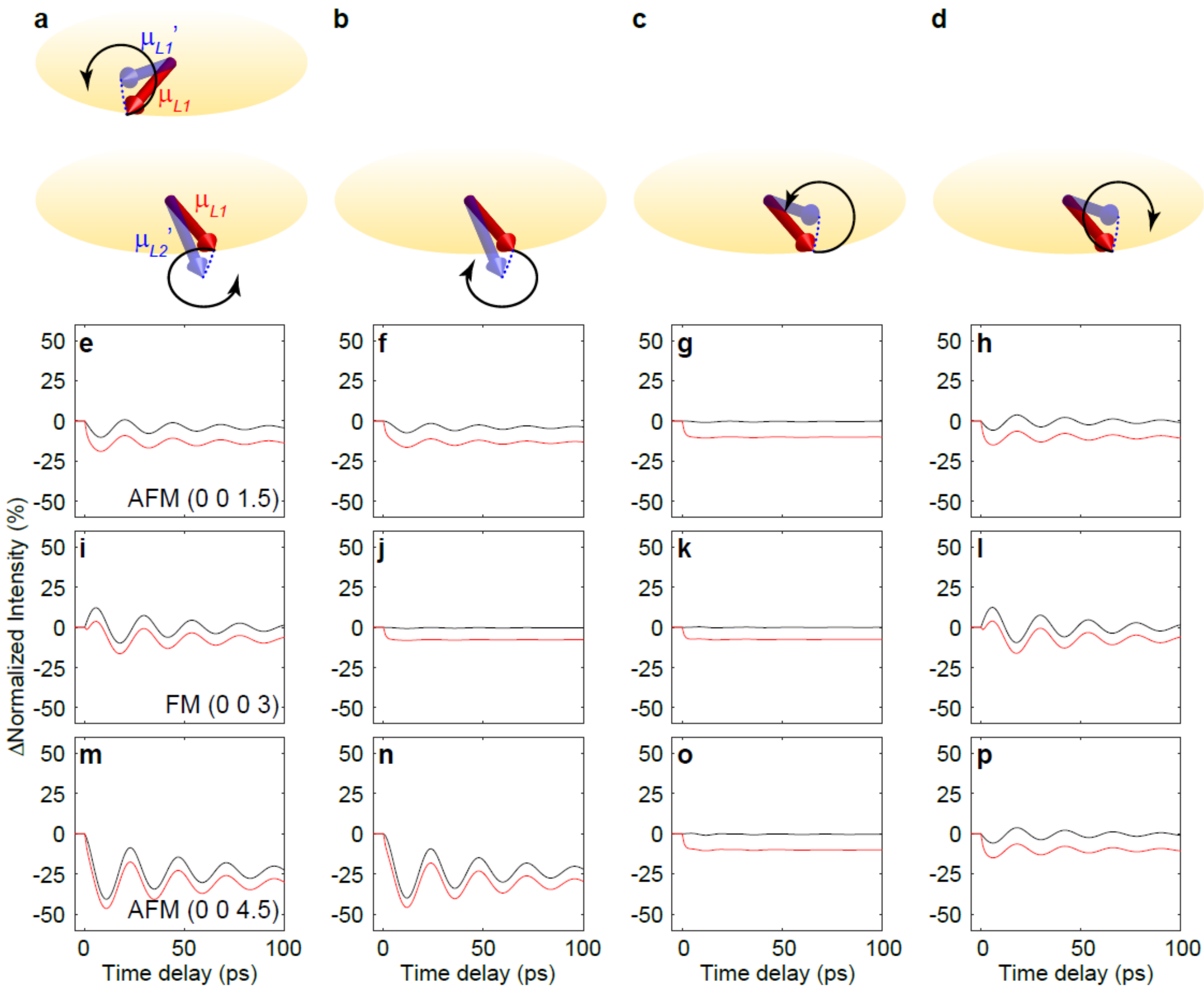

Supplementary Fig. 8| Simulated transient behaviours of the FM and AFM Bragg reflections for the case where μ_{L1} precesses counter-clockwise around a new quasi-equilibrium μ_{L1}' direction located out of the *xy* plane. (**a**) Counter-clockwise and (**b**) clockwise μ_{L2} precessions around μ_{L2}' moved opposite to μ_{L1}' along the *z* axis. (**c**) Counter-clockwise and (**d**) clockwise μ_{L2} precessions around μ_{L2}' moved in the same direction with μ_{L1}' along the *z* axis. The red, blue, and black arrows denote μ_L, μ_L', and precession directions, respectively. The transient intensities of (**e-h**) AFM (0 0 1.5), (**i-l**) FM (0 0 3), and (**m-p**) AFM (0 0 4.5) Bragg peaks for the cases illustrated in (**a-d**), respectively. The intensities are normalized with the one at a negative time delay. Black (red) curves present the simulation results without (with) initial demagnetization, respectively.

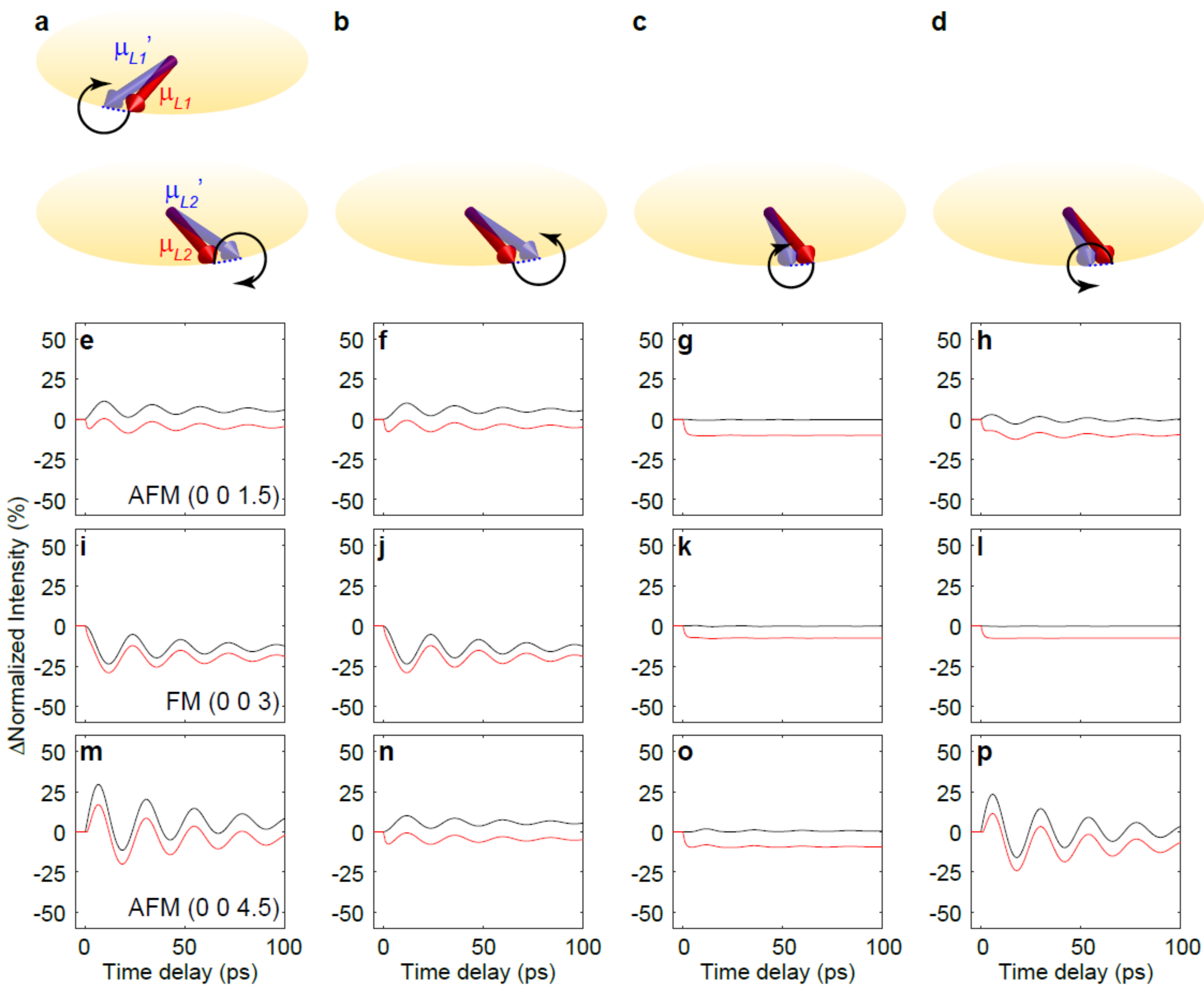

Supplementary Fig. 9| Simulated transient behaviours of the FM and AFM Bragg reflections for the case where μ_{L1} precesses clockwise around a new quasi-equilibrium μ_{L1}' direction moved within the *xy* plane and tilted away from the *x* axis. (**a**) Clockwise and (**b**) counter-clockwise μ_{L2} precessions around μ_{L2}' moved opposite to μ_{L1}' tilted away from the *x* axis. (**c**) Clockwise and (**d**) counter-clockwise μ_{L2} precessions around μ_{L2}' moved in the same direction with μ_{L1}' tilted away from the *x* axis. The red, blue, and black arrows denote μ_L, μ_L', and precession directions, respectively. The transient intensities of (**e-h**) AFM (0 0 1.5), (**i-l**) FM (0 0 3), and (**m-p**) AFM (0 0 4.5) Bragg peaks for the cases illustrated in (**a-d**), respectively. The intensities are normalized with the one at a negative time delay. Black (red) curves present the simulation results without (with) initial demagnetization, respectively.

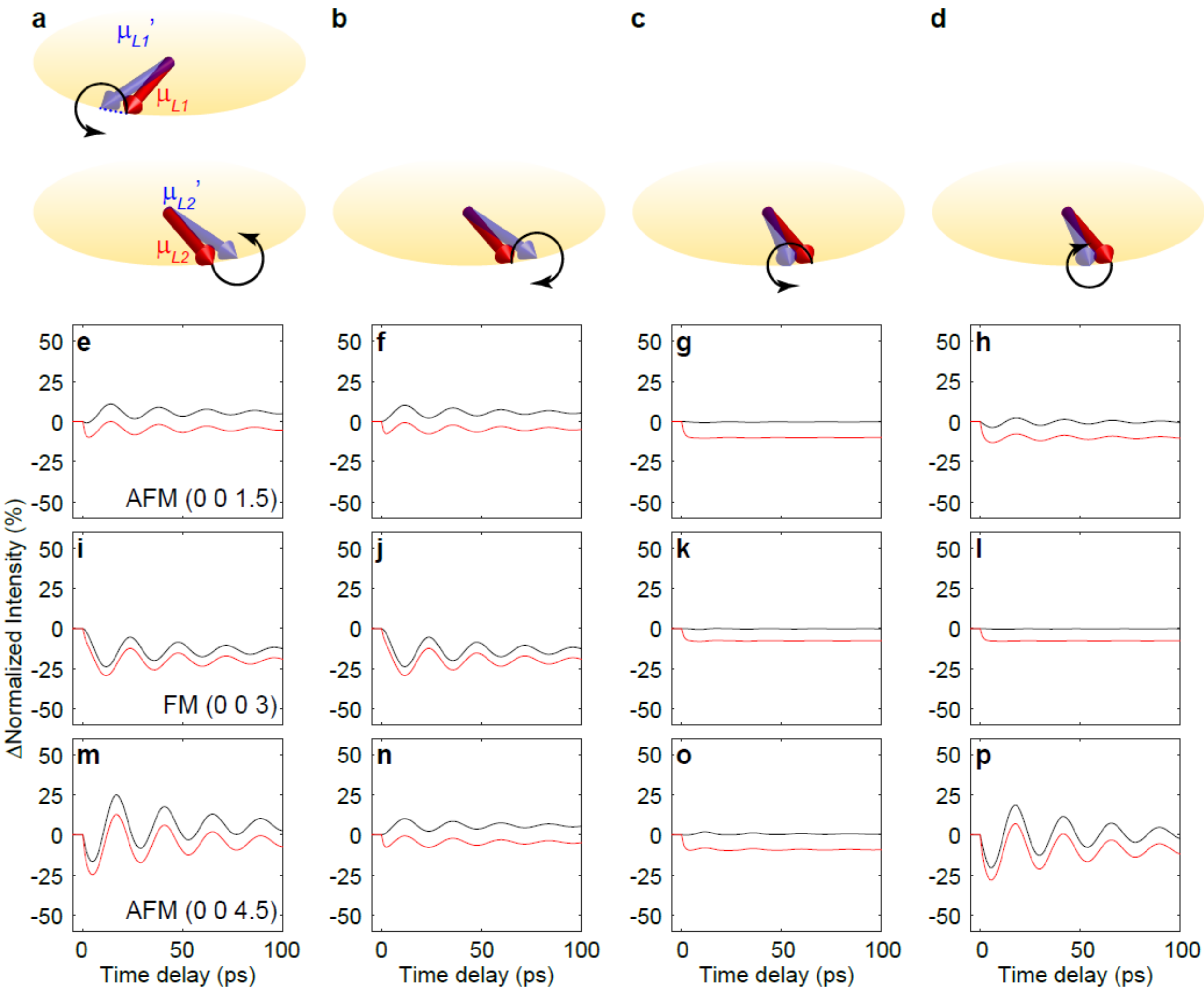

Supplementary Fig. 10| Simulated transient behaviours of the FM and AFM Bragg reflections for the case where μ_{L1} precesses counter-clockwise around a new quasi-equilibrium μ_{L1}' direction moved within the *xy* plane and tilted away from the *x* axis. (**a**) Counter-clockwise and (**b**) clockwise μ_{L2} precessions around μ_{L2}' moved opposite to μ_{L1}' tilted away from the *x* axis. (**c**) Counter-clockwise and (**d**) clockwise μ_{L2} precessions around μ_{L2}' moved in the same direction with μ_{L1}' tilted away from the *x* axis. The red, blue, and black arrows denote μ_L, μ_L', and precession directions, respectively. The transient intensities of (**e-h**) AFM (0 0 1.5), (**i-l**) FM (0 0 3), and (**m-p**) AFM (0 0 4.5) Bragg peaks for the cases illustrated in (**a-d**), respectively. The intensities are normalized with the one at a negative time delay. Black (red) curves present the simulation results without (with) initial demagnetization, respectively.

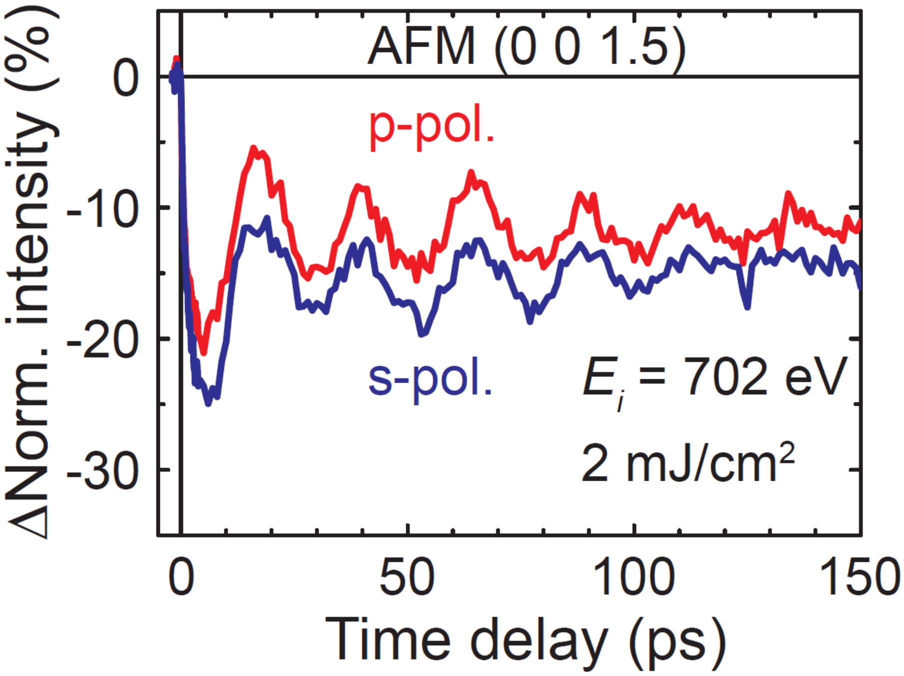

Supplementary Fig. 11| Transient change of the normalized AFM (0 0 1.5) peak intensity by the pump laser with *p*- and *s*-polarizations. The data for *p*-polarization (red) and *s*-polarization (blue) were obtained for the laser fluence = 2.0 mJ/cm^2 at T = 82 K under H_{ext} = 200 mT applied along the x axis in the ab plane. The incident photon energy E_i = 702 eV was used to observe the bulk-sensitive signal.

	A_1	A_2	A_3	τ_1 (ps)	τ_2 (ps)	t_1 (ps)	Ω (ps)
(0 0 1.5)	0.06	0.07	1.00	119.77	2.81	12.18	23.96
(0 0 3)	0.06	0.02	0.94	106.47	22.09	18.85	24.07
(0 0 4.5)	0.10	-	0.99	107.39	-	12.38	24.24

Supplementary Table S1| The fitting parameters for the transient Bragg peak intensities in Figs. 2a-c (the main text). The A_2 for the AFM (0 0 4.5) Bragg peak is negligible making τ_2 undefined.